# Binary Au-Cu reaction sites decorated ZnO for selective methane oxidation to C1 oxygenates with nearly 100% selectivity at room temperature

Lei Luo[a], Zhuyu Gong[a], Youxun Xu[b], Jiani Ma[a], Huifen Liu[a], Jialiang Xing[a], Junwang Tang[b]*

[a] Key Lab of Synthetic and Natural Functional Molecule Chemistry of Ministry of Education, the Energy and Catalysis Hub, College of Chemistry and Materials Science, Northwest University, Xi'an, 710127, P. R. China.

[b] Department of Chemical Engineering, University College London, Torrington Place, London WC1E 7JE, UK.

* Corresponding author: junwang.tang@ucl.ac.uk

**ABSTRACT**

Direct and efficient oxidation of methane to methanol and the related liquid oxygenates provides a promising pathway for sustainable chemical industry, while still remains an ongoing challenge owing to the dilemma between methane activation and over-oxidation. Here, ZnO with highly dispersed dual Au and Cu species as cocatalysts enables efficient and selective photocatalytic conversion of methane to methanol and one-carbon oxygenates using $O_2$ as the oxidant operated at ambient temperature. The optimized AuCu-ZnO photocatalyst achieves up to 11225 $\mu mol \cdot g^{-1} \cdot h^{-1}$ of primary products ($CH_3OH$ and $CH_3OOH$) and HCHO for 2 h reaction with a nearly 100% selectivity, resulting into 14.1 % apparent quantum yield at 365 nm, much higher than the previous best photocatalysts reported for methane conversion to oxygenates. In-situ EPR and XPS disclose that Cu species serve as photo-induced electron mediators to promote $O_2$ activation to ·OOH, simultaneously Au as an efficient hole acceptor to enhance $H_2O$ oxidation to ·OH, thus synergistically promoting charge separation and methane transformation. This work highlights the significances of co-modification with suitable dual cocatalysts on simultaneous regulation of activity and selectivity.

**KEYWORDS**: methane conversion, dual cocatalysts, selective oxidation, photocatalysis, room temperature.

## INTRODUCTION

Methane is viewed as the most abundant building block for chemical synthesis due to its extremely high reserve and low price. [1-6] However, its direct combustion as a fuel or emission to environment causes either energy-wasting or environmental issues. [7-11] Upgrading alkane including methane to higher-value oxygenates such as methanol is a promising route to realize sustainable chemical industry. [12-14] The current industrial methane conversion process undergoes indirect multi-step procedure, accompanied by thermochemical operation at high temperature (> 700 ºC) which is energy-intensive and unfavorable for the sustainable development. Due to the high dissociation energy of the first C-H bond in methane and easy over-oxidation of the oxygenate products, direct conversion of methane into high-value-added chemicals like methanol and formaldehyde suffers from either inadequate activity or selectivity [15-19]. Thus, it is of great significance to explore economic and environmentally friendly routes for direct methane conversion to value-added chemicals under mild conditions.

Photocatalysis has emerged as an unprecedented approach for overcoming thermodynamic barrier and facilitating energy storage or selective methane conversion, especially under mild conditions [4, 20-30]. Efficient separation of charge carrier and proper surface reaction kinetics are the key factors to promote methane activation as well to inhibit over-oxidation of the desired products. Utilizing $FeO_x/TiO_2$ photocatalysts with $H_2O_2$ oxidants, up to 90 % methanol selectivity under ambient conditions was reported. [31] High yield (250 μmol) of one-carbon oxygenates was achieved over noble-metal modified ZnO. [32] Besides, formaldehyde [33, 34], ethane [35-39] and ethanol [40] were also acquired in various distinctive photocatalytic systems. Such representative efforts encourage more rational designs particularly on surface engineering and suitable cocatalysts development, however confronting great challenges on simultaneously optimizing activity and selectivity.

Suitable cocatalysts are the key to both promote charge separation and regulate surface catalytic reaction. Combined with the conduction band (CB), noble metal clusters usually serve as electron acceptors via Schottky heterojunction or induce surface plasmon resonance effect, respectively [41, 42]. On the other hand, transition metal oxides like cobaltous oxide ($CoO_x$) could serve as the hole acceptor from the valence band (VB) [43]. The integration of both electron acceptor and donor cocatalysts with the photocatalyst could boost charge separation and weaken the oxidative potentials of photocatalysts to suppress over-oxidation. Given this very attractive potential, there are few reports

on immobilization of binary cocatalysts with complementary function on a photocatalyst. Besides, highly dispersed cocatalysts are also desired to maximize metal-support interaction and enable distinctive reaction pathways to tune selectivity [44-49]. Moreover, $H_2O$ is widely accepted as one of the most environmentally benign and commercially available solvent than many organics and strong corrosive acids [50]. Reaction in the presence of $H_2O$ could even inhibit over-oxidation to some extent by promoting desorption of oxygenates [51, 52].

Herein, Au and $CuO_x$ cocatalysts were designed to modify ZnO photocatalysts (denoted as $Au_xCu_y$-ZnO) to achieve the above mentioned potential, then employed in aqueous photocatalytic methane conversion with $O_2$ as the only oxidant. A high yield of the primary oxidized products (17776.8 $\mu mol \cdot g^{-1}$) with selectivity of nearly 100 % has been achieved over the optimized $Au_{0.2}Cu_{0.15}$-ZnO photocatalyst. Mechanistic studies revealed that Au and $CuO_x$ cocatalysts acted as the hole and electron acceptors, respectively, for synergistically enhancing charge separation and promoting reactant activation. Furthermore highly dispersed cocatalysts additionally adjusted the generation of reactive ·OOH and ·OH species and contributed to the improved selectivity of primary products.

## RESULTS AND DISCUSSIONS

### Photocatalytic methane conversion

Binary cocatalysts modified ZnO photocatalysts were prepared through the modified hydrothermal method [53]. Certain amount of Au and $CuO_x$ were simultaneously deposited on ZnO with hydrogen tetrachloroaurate(III) ($HAuCl_4$), copper dichloride ($CuCl_2$) as the precursors and ascorbic acid as reduction agents, respectively. The as-prepared photocatalysts were denoted as $Au_xCu_y$-ZnO, where x % and y % represented the mass percent of Au and Cu dosage on the ZnO substrate. The actual metal content was measured by inductively coupled plasma atomic emission spectrometer (ICP-AES). For comparison, single cocatalyst modified ZnO photocatalysts (including $Au_x$-ZnO and $Cu_{0.15}$-ZnO) were also prepared.

Photocatalytic activity was primarily screened by methane conversion conducted in a top-irradiation high-pressure batch reactor where 20 mg photocatalyst particles were suspended in 100 mL distilled water at 25 °C for 2 h irradiation in a mixture of 19 bar $CH_4$ and 1 bar $O_2$. Control experiments were also carried out (**Table S1**). No products detected in these control experiments suggested the crucial role of both photocatalyst and light irradiation. **Figure 1a** presented the average oxygenates production, including $CH_3OH$, $CH_3OOH$ and HCHO together with $CO_2$ over ZnO and

$Au_x$-ZnO photocatalysts. The former two oxygenates were regarded as the primary products in methane conversion, while HCHO and $CO_2$ were over-oxidized products [19, 43]. Only trace amount of $CO_2$ was detected for almost all photocatalysts, demonstrating the high selectivity of one-carbon (C1) oxygenates. Meanwhile, ZnO exhibited a relatively low C1 oxygenate yield of 2403.5 $\mu mol \cdot g^{-1}$ for two hour reaction (24.0 $\mu mol \cdot h^{-1}$), consistent with the severe charge recombination in pristine ZnO nanocrystals. After incorporating Au, productions of C1 oxygenates were dramatically improved, exhibiting a volcanic trend with increasing Au loading gradually. The highest production of C1 oxygenates reached 7749.3 $\mu mol \cdot g^{-1}$ for two hours (77.5 $\mu mol \cdot h^{-1}$) over $Au_{0.2}$-ZnO, almost 3.2 times that of ZnO. Further increasing Au content caused the decrease of photocatalytic C1 production, which was attributed to the shielding effect [54] or increased size of Au from 31.9 nm to 57.8 nm (**Figure S1**). The optimized Au size was 41.9 ± 17.6 nm with Au content of 0.2 wt.%. The selectivity of the primary products ($CH_3OH$ and $CH_3OOH$) for $Au_x$-ZnO was also improved and exhibited a volcanic trend with the highest selectivity achieved on $Au_{0.2}$-ZnO (60.9 %). Au was reported to serve as the electron or hole acceptors [55-57], it thus contributed to the enhanced charge separation efficiency and promoted $CH_4$ conversion. The actual effect of Au on the binary cocatalysts system will be discussed in the mechanism study section.

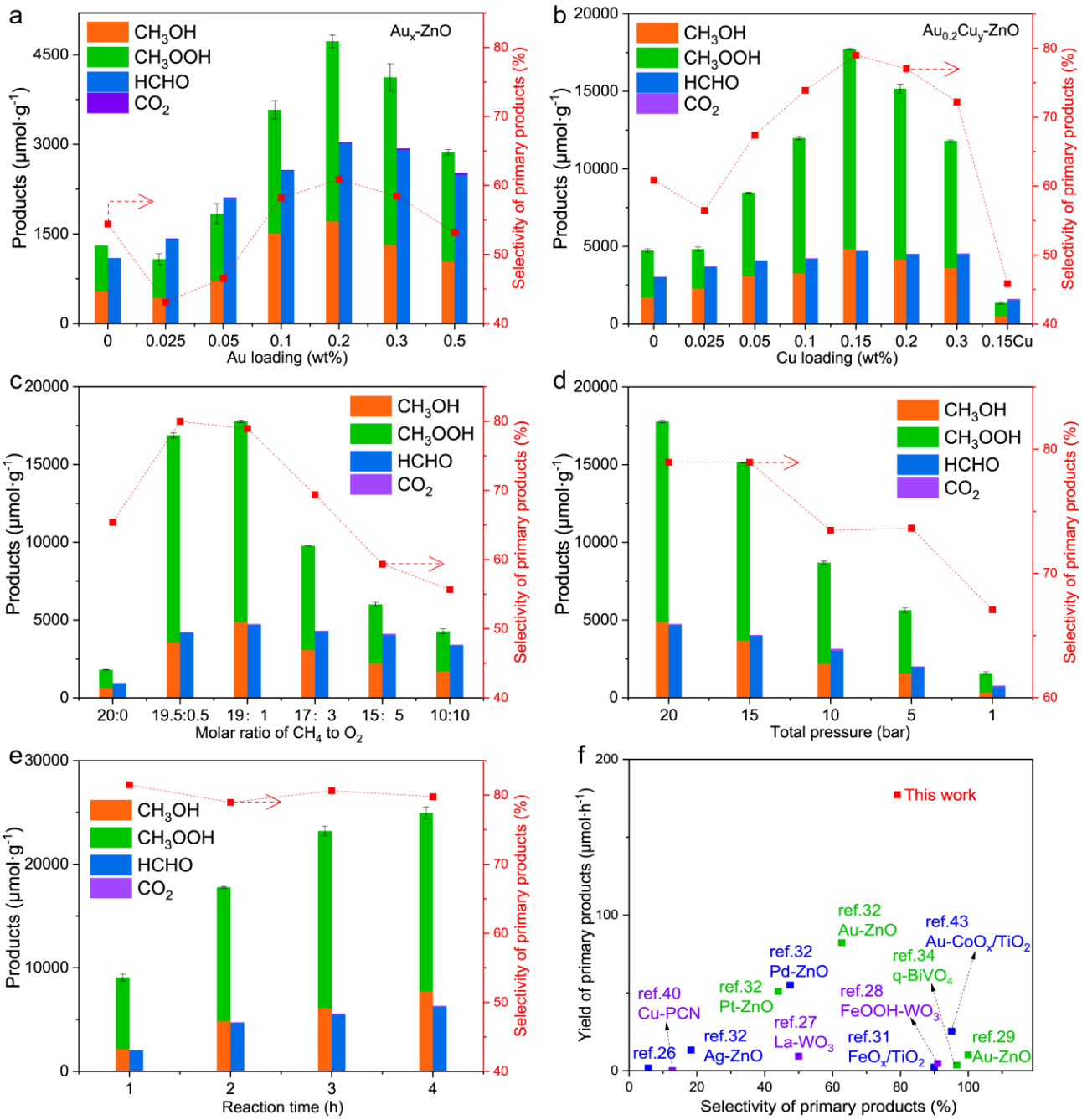


**Figure 1.** Photocatalytic direct methane conversion and the selectivity of the primary products ($CH_3OH$ and $CH_3OOH$) over (a) $Au_x$-ZnO for Au content optimization, (b) $Au_{0.2}Cu_y$-ZnO for Cu content optimization with constant 0.2 wt.% Au, c) molar ratio of $CH_4$ to $O_2$ and (d) total pressure change. Reaction conditions: 20 mg photocatalyst, 100 mL $H_2O$, 1 bar $O_2$, 19 bar $CH_4$, 25 °C, 2 h, 300 W Xe lamp. Investigations on (e) reaction time over the optimized $Au_{0.2}Cu_{0.15}$-ZnO photocatalyst. (f) Comparisons with the representative photocatalytic performances on the yield per hour and selectivity of the primary products ($CH_3OH$ and $CH_3OOH$).

To further enhance charge separation and optimize the surface reaction kinetics, copper was introduced which was regarded as the critical component of the monooxygenase enzyme for

biocatalytic methane conversion in nature [8, 58]. Compared with $Au_{0.2}$-ZnO, both the production of oxygenates and the selectivity of the primary products were remarkably improved on the binary $Au_{0.2}Cu_y$-ZnO photocatalysts (**Figure 1b**), demonstrating the efficiency of copper oxides ($CuO_x$) decoration. Along with Cu content rising, the C1 production increased, and reached the highest value over $Au_{0.2}Cu_{0.15}$-ZnO at 22449.8 μmol·$g^{-1}$ after the two-hour reaction (224.5 μmol·$h^{-1}$), about 9.3 and 3 times improvements than that of ZnO and $Au_{0.2}$-ZnO, respectively. Further increasing the loading of Cu caused a decreased photocatalysis due to the shielding effect [54]. Meanwhile, the selectivity of the desired products also exhibited volcanic trend along with the activity. For $Au_{0.2}Cu_{0.15}$-ZnO, the highest selectivity was achieved up to ca. 80 %, much higher than the pristine and single cocatalysts modified ZnO. A low C1 production of 2895.0 μmol·$g^{-1}$ for the two-hour reaction (29.0 μmol·$h^{-1}$) was determined on $Cu_{0.15}$-ZnO with single $CuO_x$ cocatalyst. With a close observation of the photocatalytic performance, the binary Au-$CuO_x$ cocatalysts exhibited 2.1 times higher activity than sum of the single cocatalyst loaded photocatalyst, demonstrating the synergistic effect of the binary cocatalysts on methane activation. With a constant mass ratio of Au to Cu of 4:3, the total content effect of Au-$CuO_x$ cocatalysts on methane oxidation was investigated (**Figure S2**). The results demonstrated that $Au_{0.2}Cu_{0.15}$-ZnO exhibited the highest activity, with the selectivity nearly unchanged. Further increasing the total content of dual-cocatalysts led to the weakened photocatalytic performances after the optimal content, which would be caused by the enlarged particle size of Au from 5.1 nm to 8.4 nm (**Figure S3** and **Figure S4**). Compared with $Au_{0.2}$-ZnO, it indicated that the addition of Cu during hydrothermal synthesis also suppressed the Au particle growth. In addition, to work out the influence of Au particle size, $Au_{0.2}$-ZnO(PD) with the average Au particle size of 7.4 nm (**Figure S5**) was prepared and evaluated for photocatalytic $CH_4$ conversion under identical experimental conditions. One can see in **Figure S6** that $Au_{0.2}$-ZnO(PD) exhibited a higher photocatalytic $CH_4$ conversion activity than $Au_{0.2}$-ZnO, with the yield of oxygenates improved from 7749.3 μmol·$g^{-1}$ to 10305.5 μmol·$g^{-1}$, suggesting the positive effect of the reduced nanoparticle size that could provide more reactive sites for $H_2O$ oxidation to generate ·OH and then to activate $CH_4$. In spite of this, the yield of oxygenates by $Au_{0.2}Cu_{0.15}$-ZnO was still 2.2 times higher than $Au_{0.2}$-ZnO(PD), indicating that the dramatic improvement of $CH_4$ conversion was mainly originated from the synergy of Au and Cu. Such promoted effect on the photocatalytic $CH_4$ conversion was also supported by the other two case studies, where the bimetallic AuCu cocatalysts was loaded on anatase $TiO_2$ or P25 as shown in the supporting information (**Figure S7**). Anatase $TiO_2$ exhibited a relatively

low yield of oxygenates (1255.0 μmol·$g^{-1}$), with a selectivity of the primary products ($CH_3OH$ and $CH_3OOH$) of 73.3 %. For Au-$TiO_2$ and Cu-$TiO_2$, yields of oxygenates for a two-hour reaction increased to 2070.0 μmol·$g^{-1}$ and 1560.1 μmol·$g^{-1}$, respectively, exhibiting the enhancement of photocatalytic $CH_4$ conversion after single Au and Cu cocatalyst loading. In the meantime, the selectivity of the primary products also increased to 76.8 % on Au-$TiO_2$ and 77.8 % on Cu-$TiO_2$. The integration of both Au and Cu further boosted the photocatalysis, with the highest yield of oxygenates for a two-hour reaction reaching 2690.0 μmol·$g^{-1}$ and the selectivity of primary products up to 81.8 %. Similarly, three photocatalysts on P25 $TiO_2$ were also prepared and used for $CH_4$ conversion. P25 exhibited higher activity than that of anatase $TiO_2$, probably attributing to the heterojunction structure in P25 existing between anatase and rutile phase. Again, the selectivity to the primary products has the same order AuCu-P25 (85.8 %) > Cu-P25 (83.1 %) > Au-P25 (81.4 %) > P25 (76.4 %). This further indicated that dual-cocatalyst modification was the best.

The molar ratio of $CH_4$ to $O_2$ was then investigated on the optimized $Au_{0.2}Cu_{0.15}$-ZnO (**Figure 1c**) with a total 20 bar pressure. Under anaerobic condition, a relatively low yield of C1 oxygenates of 2740 μmol·$g^{-1}$ after the two-hour reaction (27.4 μmol·$h^{-1}$) was gained, suggesting the crucial role of $O_2$ on promoting $CH_4$ conversion. As a comparison, the yield of oxygenates dramatically increased to the highest at $CH_4/O_2$ = 19/1. A lower $CH_4/O_2$ ratio leads to the gradually decreased yield to 7665.2 μmol·$g^{-1}$ after the two-hour reaction (76.7 μmol·$h^{-1}$) at $CH_4/O_2$ = 10/10. As $O_2$ has relatively higher solubility than $CH_4$ in $H_2O$ [59, 60], such decreased overall yield was mainly ascribed to the dramatically decreased concentration of $CH_4$ reactant dissolved in water under decreased $CH_4$ pressure. The selectivity of the primary products also decreased with the decrease of $CH_4/O_2$ ratio, which probably caused by the increased concentration of $O_2$ that inducing over-oxidation to HCHO.

When simultaneously decreasing the concentration of $CH_4$ and $O_2$ under a constant molar ratio (19:1) through lowering total pressure (**Figure 1d**), the production of oxygenates after the two hour reaction gradually decreased from 22450 μmol·$g^{-1}$ (224.5 μmol·$h^{-1}$) at 20 bar to 2267 μmol·$g^{-1}$ (22.7 μmol·$h^{-1}$) at the ambient pressure. According to the Raoult's law, it demonstrated that the concentration of the dissolved $CH_4$ and $O_2$ in $H_2O$ plays the critical role in promoting $CH_4$ conversion herein. When prolonging the reaction time up to 4 h (**Figure 1e**), the production of the primary products for the two-hour reaction improved to 31200 μmol·$g^{-1}$ (312.0 μmol·$h^{-1}$), while the selectivity remained nearly unchanged.

The amount of $H_2O$ was also investigated and shown in **Figure S8**. With the increase of $H_2O$

dosage, the yield of oxygenates for the two-hour reaction gradually increased from 5383 μmol·$g^{-1}$ (53.8 μmol·$h^{-1}$) for 25 mL to 22449 μmol·$g^{-1}$ (224.5 μmol·$h^{-1}$) for 100 mL water. The selectivity of the primary products was also improved from 60.4 % to 78.9 %. Such enhanced photocatalysis could be attributed to the enhanced desorption of oxygenate products from the surface due to enhanced mass transfer introduced by water solvent. In parallel, $CH_4$ conversion reaction without $H_2O$ as a solvent in the reactor was also conducted. In this case, photo-induced $h^+$ was the main oxidative specie. Meanwhile, the exposed surface of photocatalyst in the absence of $H_2O$ might be beneficial to adsorb $CH_4$ due to its low solubility in water and would achieve enhanced photoactivity. However, only $CO_2$ was produced with a yield of 252.9 μmol·$g^{-1}$, indicating that photoholes would directly overoxidize $CH_4$ to $CO_2$. Moreover, when using $CH_3CN$ as an inert solvent instead of $H_2O$, though the solubility of $CH_4$ greatly improved, the photocatalytic results showed that only trace amount of oxygenates (2.7 μmol·$h^{-1}$ of $CH_3OH$ and 6.5 μmol·$h^{-1}$ of $C_2H_5OH$) were produced under identical conditions. Such suppressed activity in the absence of $H_2O$ or replacement of organic solvents demonstrated $H_2O$ promoted the activation of $CH_4$, and more importantly suppressed oxygenate products from over-oxidation. Three possible reasons would contribute to such effect of $H_2O$ on suppressing over-oxidation. In the presence of $H_2O$, ·OH radicals instead of photoholes were the major species to activate methane, which had a relatively weaker oxidative ability than that of photoholes. Next superoxide radicals ($\cdot O_2^-$) with strong oxidative ability that produced from the reduction of $O_2$ with photo-induced electrons would combine with $H^+$ from $H_2O$ to get ·OOH ($O_2 + e^- + H^+ \rightarrow \cdot OOH$), which is a milder reactive specie than $\cdot O_2^-$ [32]. Lastly, the competitive adsorption of $H_2O$ with $CH_3OH$ on the surface of photocatalysts could promote the desorption of the as-produced $CH_3OH$ to some extent, and thus avoiding deep oxidation.

The stability of the best catalyst $Au_{0.2}Cu_{0.15}$-ZnO was then investigated. It exhibited excellent stability, which was evaluated by the five measurements as well as XRD, XPS and HRTEM characterizations. The performances of five runs were shown in **Figure S9**. The production and selectivity of oxygenates after the two-hour reaction remained identical with a high yield of ca. 22000 μmol·$g^{-1}$ and ca. 80 % selectivity of the primary products. Such excellent stability of $Au_{0.2}Cu_{0.15}$-ZnO was also supported by the same XRD patterns and XPS spectra of the fresh and used photocatalysts (**Figure S10**). In the meantime, the size distribution of Au for the used $Au_{0.2}Cu_{0.15}$-ZnO was measured, which was 5.9 ± 1.6 nm (**Figure S11**) and remained nearly unchanged after five consecutive runs. Au nanoparticles were also reserved the good crystallinity with the crystal plane distance being indexed

to (111) and (200) facets. EDS-mapping images showed the uniform distribution of Cu with no obvious nanoparticles observed, suggesting the high dispersion of Cu species was reserved after the reaction. Such stable Au and Cu species were the active structures that contributed to the stable photocatalysis.

To avoid misleading on the normalized mass product rates, we converted all reported results on methane oxidation to the similar primary products to the unit of molar amount per hour and summarized the photocatalytic methane conversion on the representative catalysts in **Figure 1f**. Some of the photocatalysts like $FeO_x/TiO_2$, FeOOH-$WO_3$, q-$BiVO_4$, Au-$CoO_x/TiO_2$ and Au-ZnO exhibited a higher selectivity of the primary products (> 90 %) than ours while an extremely low yield (< 25.4 $\mu mol \cdot h^{-1}$) was reported, which is nearly 9 times slower than ours. As a comparison, noble metal (Pd, Pt, Au) modified ZnO photocatalysts showed a good production rate (about 82.3 $\mu mol \cdot h^{-1}$) of the primary products, while the selectivity (44~62 %) still had a large room to be improved. One can see due to different experiment conditions used including the light intensity, co-catalyst loading amount and the photocatalyst concentration in the literatures, oxygenates yields reported varied from the production of 10.2 $\mu mol \cdot h^{-1}$ on $Au_{0.15}$/ZnO [29] to 131.5 $\mu mol \cdot h^{-1}$ on 0.1 wt% Au/ZnO [32]. In this work the reference single Au cocatalysts modified ZnO ($Au_{0.2}$-ZnO) exhibited a moderate yield of oxygenates at 77.5 $\mu mol \cdot h^{-1}$, lower than the highest reported before [32]. Despite of this, $Au_{0.2}Cu_{0.15}$-ZnO prepared in this work exhibited a superior yield of 224.5 $\mu mol \cdot h^{-1}$ of all oxygenates, much higher than the previous benchmark result. In parallel, the selectivity of C1 oxygenates (including $CH_3OH$, $CH_3OOH$ and HCHO) reached nearly 100 % and the selectivity to the primary products was ca. 80 %. Moreover, the apparent quantum yield (AQY) is a widely accepted criterion for fairly evaluating the efficiency of a photocatalyst while it was not reported in many literatures in this research area. The AQY was measured as 14.1 % at 365 ± 10 nm for $Au_{0.2}Cu_{0.15}$-ZnO, which was again much higher than all systems reported (**Table S2**).

**Structural identification of $Au_xCu_y$-ZnO photocatalysts**

X-ray diffraction (XRD) patterns (**Figure 2a**) indicated the typical ZnO structure of the as-prepared photocatalysts. Characteristic diffraction peaks of ZnO (PDF#36-1451) without any peak offset suggested the well-crystallized phase during hydrothermal synthesis. No diffraction peaks that could be assigned to Au or Cu associated phases were observed, which was probably due to their very low amount. The actual Au and Cu loadings were then measured by ICP-AES. For $Au_{0.2}Cu_{0.15}$-ZnO, the

measured Au and Cu contents were 0.24 wt.% and 0.06 wt.%, respectively. $Au_{0.2}$-ZnO and $Cu_{0.15}$-ZnO separately contained the identical content of Au and Cu to that of $Au_{0.2}Cu_{0.15}$-ZnO. Nitrogen physical sorption results exhibited the similar specific surface area of 21.1, 22.8, 26.5 and 28.3 $m^2/g$ for ZnO, $Au_{0.2}$-ZnO, $Cu_{0.15}$-ZnO and $Au_{0.2}Cu_{0.15}$-ZnO, respectively. Raman spectra (**Figure 2b**) further supported the typical ZnO structure of the photocatalysts. For ZnO, peaks were clearly observed at 329.2 $cm^{-1}$, 437.5 $cm^{-1}$ and 581.1 $cm^{-1}$, respectively. For the cocatalysts modified photocatalysts, the characteristic Raman peaks exhibited a slight noisy and left-shift from 437.5 $cm^{-1}$ to 435.0-436.7 $cm^{-1}$ and from 581.1 $cm^{-1}$ to 572.2 $cm^{-1}$, which could be arisen from the surface strain effect after cocatalyst modification [61].

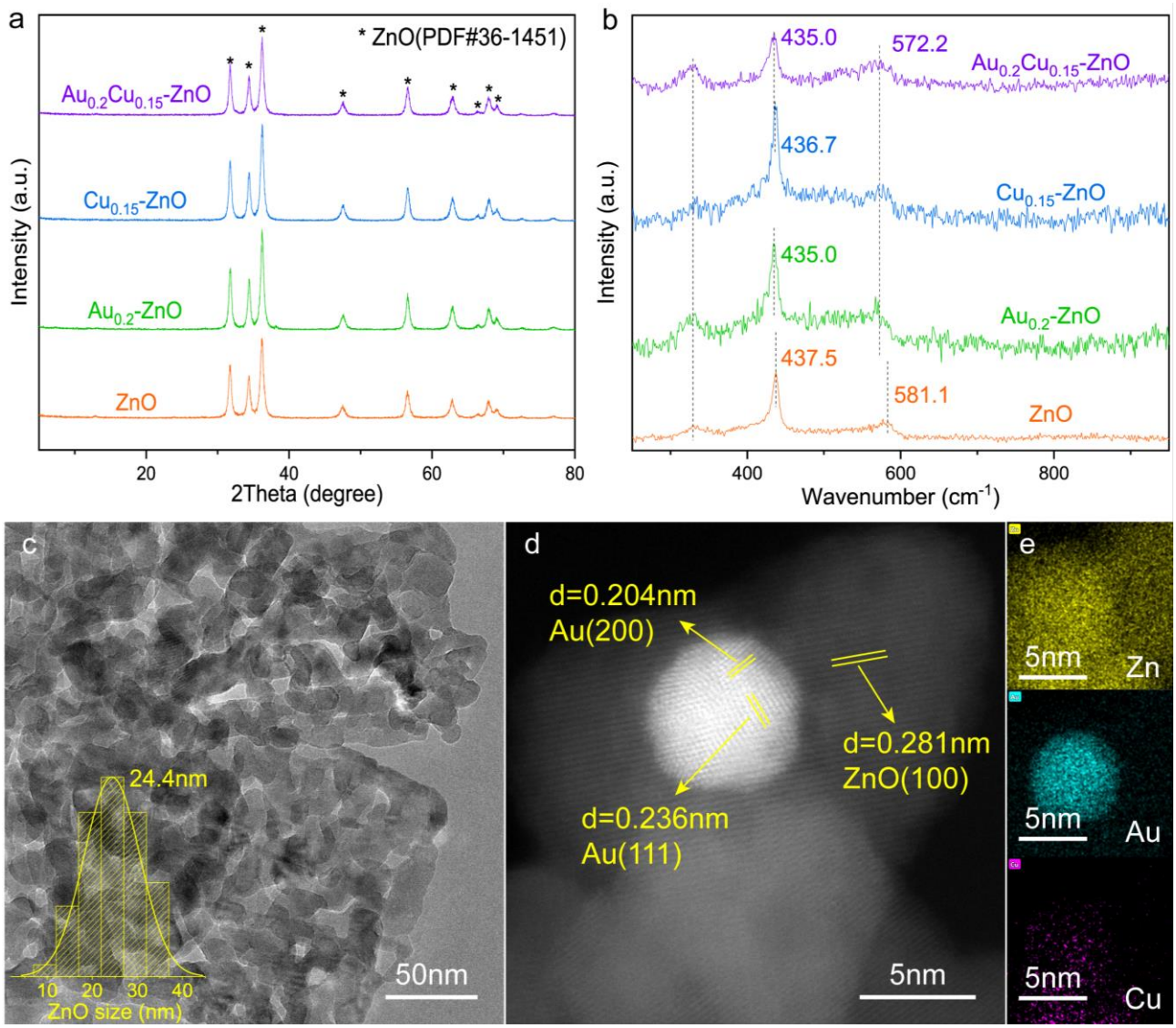


**Figure 2.** (a) XRD patterns and (b) Raman spectra of ZnO, $Au_{0.2}$-ZnO, $Cu_{0.15}$-ZnO and $Au_{0.2}Cu_{0.15}$-ZnO. (c) TEM images of ZnO. (d) HAADF-STEM and (e) EDS-mapping images of $Au_{0.2}Cu_{0.15}$-ZnO. The inset of c shows the particle size distribution of ZnO. Yellow, blue and pink colors in e represent

Zn, Au and Cu elements, respectively.

Aberration corrected high-angle annular dark field scanning transmission electron microscope (HAADF-STEM) images (**Figure 2d**) of the tailored $Au_{0.2}Cu_{0.15}$-ZnO hybrid exhibited the crystalline fringe of 0.281 nm, which could be assigned to the (100) facet of ZnO substrate with an average particle size of 24.4 ± 6.1 nm (**Figure 2c**). Meanwhile, the crystalline fringes of 0.204 and 0.236 nm were also found and attributed to the (200) and (111) facets of the supported Au cocatalyst, respectively. The average diameter of Au nanoparticles was measured as 5.8 ± 1.8 nm as shown in the inset of **Figure S12**. No obvious $CuO_x$ clusters were found, suggesting its very high dispersion and sub-nanosized characteristic. Elemental distribution in the corresponding area was observed by EDS-mapping images and shown in **Figure 2e**. It is clear that Au nanoparticle was supported on the ZnO substrate. Uniform distribution of Zn and Cu elements indicated the successful introduction of $CuO_x$ and its high dispersion while much smaller concentration than Au. Such high dispersed cocatalysts are beneficial to enhance interaction and decrease the interfacial charge transfer resistant. Notably, as the separate species of Au and $CuO_x$ on ZnO, the separated holes and electrons on Au and $CuO_x$ can not readily recombine as discussed later.

**Photocatalytic mechanism investigation**

Photoabsorption, charge separation and the surface reaction are the three consecutive important steps that significantly influence the photocatalysis process. UV-DRS spectra (**Figure 3a** and **Figure S13**) were conducted to evaluate the photoabsorbance of the representative photocatalysts. All photocatalysts exhibited a similar absorption edge at ca. 390-398 nm, suggesting the relatively identical structure of ZnO among the as-prepared photocatalysts. Besides, $Au_{0.2}$-ZnO and $Au_{0.2}Cu_{0.15}$-ZnO exhibited the small photoabsorption peak in the visible region (centered ca. 530 nm), was attributed to Au surface plasma absorption [42]. $Cu_{0.15}$-ZnO had no extra absorption band in the visible region, demonstrating the introduction of Cu cocatalyst had little influence on photoabsorption.

In-situ XPS spectra were carried out to evaluate the charge transfer behavior under light irradiation. As shown in **Figure 3b**, the dominant XPS at 91.25 and 88.58 eV were attributed to the $Zn_{3p1/2}$ and $Zn_{3p3/2}$ signals, respectively [44]. The peak of interest at 83.34 eV was assigned to $Au_{4f}$. Upon light irradiation, the dominant peak associated with Zn species exhibited no shift due to its large amount, while the binding energy of $Au_{4f}$ presented a left-shift to 83.55 eV. Such shift of the $Au_{4f}$ XPS peak

to higher binding energy suggested Au cocatalysts functioned as the hole acceptors under light irradiation. In the case of the $CuO_x$ cocatalysts, the $Cu_{2p3/2}$ XPS spectra (**Figure 3c**) could be divided into two peaks at 934.15 and 932.45 eV in dark, assigned to the $Cu^{2+}$ and $Cu^{+}/Cu^{0}$ species, respectively. Under light irradiation, the content of $Cu^{2+}$ dramatically decreased from 30 % in dark to 10 % under light while $Cu^{+}/Cu^{0}$ species increased from 70 % to 90 %, indicating $CuO_x$ clearly served as electron acceptors.

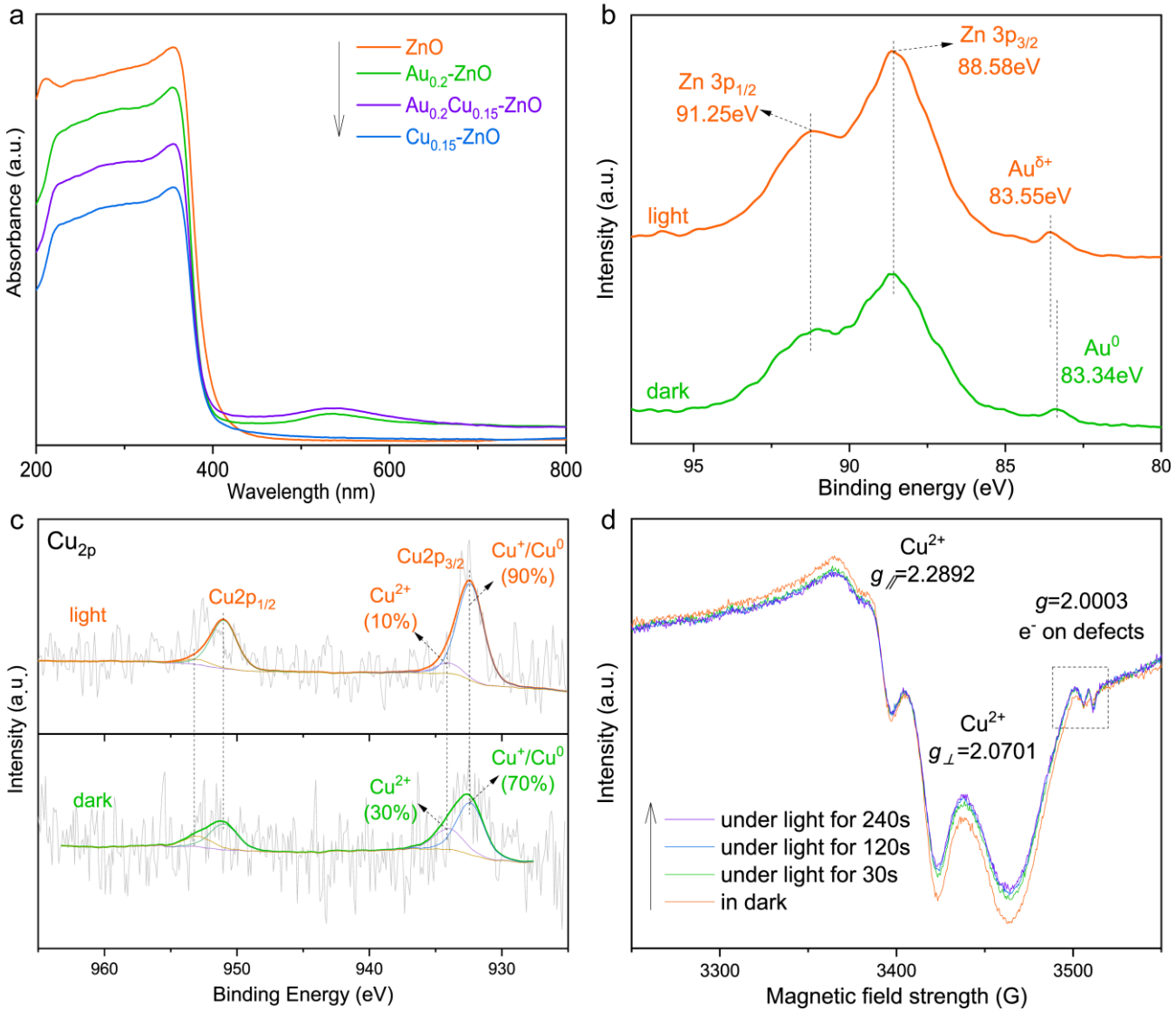


**Figure 3.** (a) UV-DRS spectra of ZnO, $Au_{0.2}$-ZnO, $Cu_{0.15}$-ZnO and $Au_{0.2}Cu_{0.15}$-ZnO. In-situ high-resolution (b) Au4f and (c) Cu2p XPS spectra of $Au_{0.2}Cu_{0.15}$-ZnO in dark and under light irradiation. (d) In-situ EPR spectra of $Au_{0.2}Cu_{0.15}$-ZnO in dark and under light irradiation.

In-situ solid-state electron paramagnetic resonance (EPR) spectra were performed to further identify the photoinduced charge dynamics of $Au_{0.2}Cu_{0.15}$-ZnO. For the pristine ZnO (**Figure S14**), a

single Lorentzian signal at $g$ = 1.9598 was observed, which was attributed to the conduction electrons captured by $Zn^{2+}$ to form $Zn^{+}$, namely trapped electron centers [62]. Under light, more and more electrons were excited from the valence band to the conduction band with increasing irradiation time and resulted in the enhanced EPR signals. In the case of $Au_{0.2}Cu_{0.15}$-ZnO, EPR signals (**Figure 3d** and **Figure S15**) were observed at $g$ = 1.9604 and 2.0003, as well $g_{\perp}$= 2.0701 and $g_{//}$ = 2.2892, attributed to the conduction electrons captured by $Zn^{2+}$, oxygen vacancies, and $Cu^{2+}$ species (**Figure 3d**), respectively [63-65]. The hyperfine EPR signals of $Cu^{2+}$ supported its high dispersion as evidenced by the EDS-mapping images. Under light irradiation, the intensity of $Cu^{2+}$ decreased, suggesting the conversion to EPR silence $Cu^{+}/Cu^{0}$, which was consistent with the in-situ XPS analysis that $CuO_x$ served as the electron acceptors. In parallel, the signal at $g$ = 1.9604 exhibits decreased intensity **(Figure S15)**, again proving that the photo-induced electrons could efficiently be transferred from the CB of ZnO to $CuO_x$. The minor EPR signal at $g$ = 2.0003 suggested the existence of defects/oxygen vacancies, which came from the reduction of ascorbic acid during hydrothermal synthesis and thus contributed to the chemical adsorption of the reactants.

Photocurrent tests (**Figure S16**) were conducted to evaluate the charge separation behavior of the photocatalysts. For the pristine ZnO, a low photocurrent density was observed at -18.1 $\mu A \cdot cm^{-2}$. After single Au cocatalyst loading, the photocurrent density exhibited 2.3 times enhancement to be -41.7 $\mu A \cdot cm^{-2}$ for $Au_{0.2}$-ZnO, demonstrating the greatly promoted charge separation. Further improved photocurrent density to -65.1 $\mu A \cdot cm^{-2}$ was found for $Au_{0.2}Cu_{0.15}$-ZnO, three times of that achieved on ZnO, indicating the most efficient charge separation induced by the binary cocatalysts. The charge separation and transfer behaviors between ZnO and cocatalysts were further investigated using steady-state PL spectra (**Figure S17)**. ZnO exhibited the band-edge emission with the strong PL emission peak at 475 nm, which correlated with the severe charge recombination of ZnO nanocrystal [56]. After the decoration with the Au cocatalyst, the PL emission peak was greatly quenched, suggesting the pronounced charge separation within $Au_{0.2}$-ZnO. The weakest PL peak observed for $Au_{0.2}Cu_{0.15}$-ZnO demonstrated its obviously suppressed charge recombination rate, which was well consistent with the photocurrent analysis and attributed to the well matched roles of electron and hole acceptors of $CuO_x$ and Au, respectively. Time-decay PL spectra (**Figure S18**) further supported the enhanced charge separation by the Au-$CuO_x$ cocatalysts. For $Au_{0.2}Cu_{0.15}$-ZnO, an average PL lifetime of 2.94 ns was determined (**Table S3**), which was longer than the others (eg. 2.23 ns for ZnO and 2.91 ns for $Au_{0.2}$-ZnO), suggesting slower kinetics of fluorescent decay which is beneficial for the

efficient separation of photogenerated charge carriers.

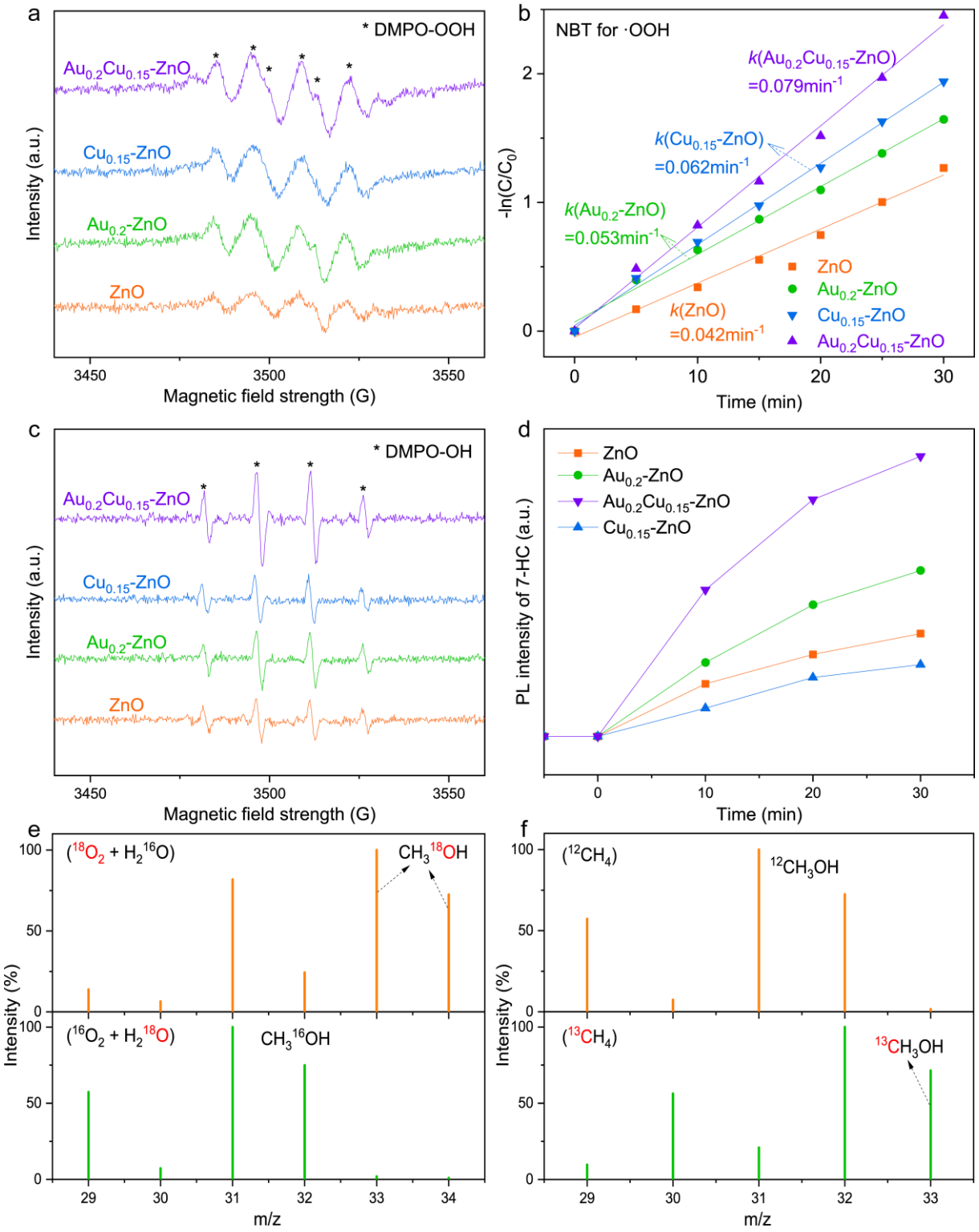


**Figure 4.** In-situ EPR spectra of (a) DMPO-OOH and (c) DMPO-OH for monitoring the generation of ·OH and ·OOH active species over different photocatalysts. (b) The kinetic constant of photodegradation of NBT for ·OOH radical detection over different photocatalysts. (d) Time-dependent PL spectra of the produced 7-hydroxycoumarin for ·OH radical detection over different

photocatalysts. GC-MS results of the isotope labeling experiments in the presence of (e) $^{16}O_2 + H_2{}^{18}O$ or $^{18}O_2 + H_2{}^{16}O$, (f) 5 bar $^{13}CH_4$ or 5 bar $^{12}CH_4$.

Following the proved complementary function of two cocatalysts for charge separation, we next investigated the reactions between the separated charges and chemical species adsorbed on the surface of the photocatalysts. Reactive oxygen species (ROS) were first monitored by in-situ EPR under light irradiation with 5, 5-dimethyl-1-pyrroline N-oxide (DMPO) as the spin-trapping agent. As shown in **Figure 4a** and **Figure 4c**, DMPO-OOH and DMPO-OH were detected in the presence of $Au_{0.2}Cu_{0.15}$-ZnO under irradiation, suggesting that ·OOH and ·OH radicals were the ROS during photocatalytic methane conversion. $Au_{0.2}Cu_{0.15}$-ZnO presented the strongest EPR intensity for both ·OOH and ·OH, indicating the highest generation of the two active species produced by $Au_{0.2}Cu_{0.15}$-ZnO. The photo-induced ROS generation ability was further evaluated with nitroblue tetrazolium chloride (NBT) and coumarin as the ·OOH and ·OH probes, respectively. **Figure 4b** and **Figure S19** presented the NBT photodegradation kinetic curves fitted with the first-order function, which was widely used for semi-quantification of $\cdot OOH/\cdot O_2^-$ generation [66]. Pristine ZnO showed the lowest first-order kinetic constant at 0.042 $min^{-1}$, while the value for $Au_{0.2}$-ZnO was larger at 0.053 $min^{-1}$. For $Au_{0.2}Cu_{0.15}$-ZnO, the highest value of 0.079 $min^{-1}$ was achieved. Therefore, it suggested that ZnO without cocatalysts modification exhibited the lowest ability to produce reactive ·OOH species from the reduction of $O_2$ molecules. Photogenerated ·OH radicals were also semi-quantified for its reactivity with coumarin to form 7-hydroxycoumain, which was shown in **Figure 4d**. After 30 min irradiation, the strong PL intensity of 7-hydroxycoumain was observed on all photocatalysts while $Au_{0.2}Cu_{0.15}$-ZnO showed the strongest, indicating the most efficient ·OH generation than the others, corresponding with the in-situ EPR results. Therefore, in the aspect of ROS generation, the introduction of binary Au-$CuO_x$ cocatalysts could rationally promote the generation of ·OOH and ·OH production, then promote $CH_4$ activation. Meanwhile, the transfer of photo-induced holes from the VB of ZnO to Au could weaken its oxidative ability and further activate $H_2O$ to ·OH, which could be beneficial to overcome deep-oxidation to other products [67], then resulting in the improved selectivity of the primary products. As the activation of the first C-H bond of $CH_4$ is difficult, the increased ·OH production over $Au_{0.2}Cu_{0.15}$-ZnO contributed to the highest photocatalytic $CH_4$ conversion to oxygenate products.

Isotopic labeling experiments with 1 bar $^{18}O_2$ and 3 mL $H_2{}^{16}O$ or 1 bar $^{16}O_2$ and 3 mL $H_2{}^{18}O$ over $Au_{0.2}Cu_{0.15}$-ZnO were carried out to investigate the oxygen source of oxygenates. As shown in **Figure 4e**, in the presence of isotopic $^{18}O_2$, $CH_3{}^{18}OH$ MS signals were observed, indicating that the formation

of $CH_3OH$ predominantly involved $O_2$ molecules as the oxygen source. Further support came from the $H_2{}^{18}O$ isotopic labelled experiment. $CH_3{}^{16}OH$ was detected as the major product, again suggesting $O_2$ molecules involved methanol production. Thus, $O_2$ acted as the predominant oxygen source for methane oxidation products [32]. $^{13}CH_4$ isotope labeling experiment (**Figure 4f)** also showed the MS signal at m/z = 33 which was ascribed to $^{13}CH_3OH$, indicating $CH_4$ serving as the carbon source to produce C1 oxygenates.

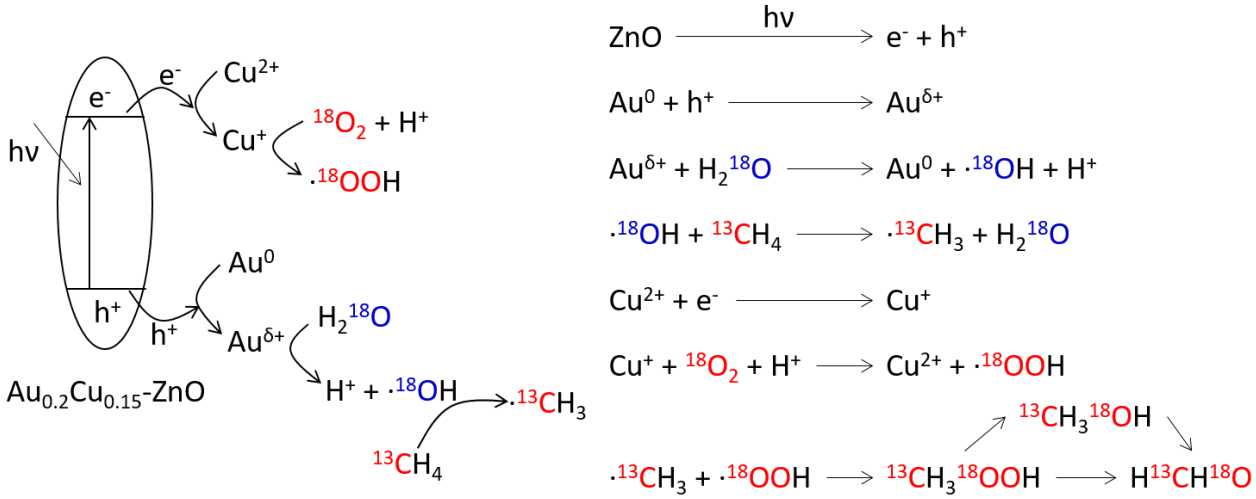


**Scheme 1**. Schematic illustration of photocatalytic methane conversion over $Au_{0.2}Cu_{0.15}$-ZnO photocatalysts.

Based on the above results, it could be seen that the introduction of Au and AuCu cocatalysts could trigger $CH_4$ activation and suppress the deep oxidation of the primary products ($CH_3OH$ and $CH_3OOH$) into HCHO and $CO_2$, where Au acted as the hole acceptor as proved by the in-situ XPS under light irradiation. ROS scavenging experiments were undertaken during $CH_4$ conversion by adding salicylic acid and $Na_2C_2O_4$ as the sacrificial agents of ·OH radicals and photoholes ($h^+$) (**Figure S20**), respectively [68, 69]. The results showed that the addition of salicylic acid almost stopped $CH_4$ conversion, more seriously than that adding the hole scavenger $Na_2C_2O_4$. Considering that ·OH was produced from the oxidation of $H_2O$ by $h^+$, such suppressed photocatalysis suggested that ·OH was the main reactive specie rather than $h^+$ for the valuable chemicals production. To selectively restore ·OH radicals, the experiment with the addition of both $Na_2C_2O_4$ and $H_2O_2$ was conducted. The yield of oxygenates was 149.0 μmol·$h^{-1}$ (24.7 μmol·$h^{-1}$ of $CH_3OH$, 88.5 μmol·$h^{-1}$ $CH_3OOH$ and 35.8 μmol·$h^{-1}$ HCHO), about 67 % of the initial activity (224.5 μmol·$h^{-1}$) was recovered.

Such predominantly recovered performance further demonstrated that ·OH was the main specie that activated $CH_4$ in this study for primary products synthesis, while photo-induced $h^+$ performed the important role in oxidation of $H_2O$ to produce ·OH radicals. To evaluate whether the as-produced $CH_3OH$ undertook deep-oxidation or decomposition, the experiment with $CH_3OH$ as a substrate was conducted (**Figure S21**). It showed that ZnO produced higher yield of HCHO (198.8 $\mu mol \cdot h^{-1}$) than that of Au-ZnO (53.7 $\mu mol \cdot h^{-1}$) with trace amount of $CO_2$ detected. Such results demonstrated that Au cocatalyst could suppress the deep oxidation of $CH_3OH$ to HCHO during $CH_4$ conversion, while decomposition of $CH_3OH$ into $CO_2$ was also suppressed. As ·OH radicals' production was more effective on Au-ZnO than ZnO as evidenced by in-situ EPR spectra and coumarin experiments, it indicated that ·OH radicals were not the main species that could induce deep oxidation of $CH_3OH$. As charge separation was enhanced by Au cocatalysts, photo-induced $h^+$ on Au tended to react with $H_2O$ to generate ·OH radicals, then led to a lower concentration of $h^+$ that could efficiently oxidize methanol to HCHO. As the binary cocatalysts greatly promoted the charge separation efficiency and accelerated both water oxidation and $O_2$ reduction, AuCu-ZnO exhibited the highest conversion of $CH_4$ to primary valuable products. Therefore, the improved selectivity of AuCu-ZnO during $CH_4$ conversion was attributed to the loading of Au that not only facilitated holes separation from electrons but also accelerated ·OH radicals production, which did not undertake overoxidation as much as photoholes. Besides the function of Au cocatalyst, water solvent played a key role on regulating the selectivity. As reported, the adsorption energies of $H_2O$ and $CH_3OH$ on Au surface were -4.07 and -3.22 eV, respectively [70, 71]. Such stronger adsorption of $H_2O$ than $CH_3OH$ on the catalyst could promote the desorption of the produced $CH_3OH$ to some extent, thus being beneficial to suppress its deep oxidation.

A tentative mechanism of photocatalytic methane conversion over $Au_{0.2}Cu_{0.15}$-ZnO was then proposed (**Scheme 1**). Upon light irradiation, electrons are generally excited to the conduction band and holes are settled on the valence band of ZnO photocatalysts. Then the hole transfers to Au cocatalysts which is supported by the in-situ XPS results, then facilitating the activation of $H_2O$ to ·OH and $H^+$, as proved by the in-situ EPR and ·OH radical measurement. The formed ·OH next activates $CH_4$ to $\cdot CH_3$, while ·OH returns to $H_2O$ and does not participate in the final oxygenate products formation. In parallel, electrons transfer to $CuO_x$ cocatalysts, where $Cu^{2+}$ is reduced to $Cu^+$, as evidenced by the in-situ EPR and XPS. $Cu^+$ next activates molecule $O_2$ and $H^+$ to form the reactive ·OOH radicals, simultaneously $Cu^+$ is back to the initial $Cu^{2+}$ states. The primary $CH_3OOH$

is formed by the radical coupling reaction between ·OOH and $\cdot CH_3$. $CH_3OOH$ then conducts a two-electron reduction process to generate $CH_3OH$. The production of HCHO from $CH_3OH$ and $CH_3OOH$ with the photogenerated hole or ·OH has been studied elsewhere [72]. Compared with $Au_{0.2}$-ZnO, the greatly enhanced generation of ·OH and ·OOH radicals are beneficial to the activation of $CH_4$ to $\cdot CH_3$ and the generation of oxygenates. Moreover, the selectivity of the desired $CH_3OH$ and $CH_3OOH$ products was tuned through the introduction of Au and Au-$CuO_x$ cocatalysts where the formation of ·OH radicals was promoted through efficient charge transfer by dual cocatalysts.

## CONCLUSIONS

In summary, through binary Au-$CuO_x$ cocatalysts modification, efficient methane activation and suppression of the over-oxidation have simultaneously been realized. Over optimized $Au_{0.2}Cu_{0.15}$-ZnO photocatalysts, the C1 oxygenate products ($CH_3OH$, $CH_3OOH$ and HCHO) were produced with a high yield of up to 11225 $\mu mol \cdot g^{-1} \cdot h^{-1}$ and ca. 100 % selectivity, a champion reported so far, resulting into 14.1 % AQY at 365 nm which is also much higher than previous benchmark work. The reason for such superior photocatalysis was explored by in-situ light-irradiated XPS and EPR spectra, which indicated that Au and $CuO_x$ efficiently served as the hole and electron acceptors, respectively to synergistically promote charge separation. $CuO_x$ furthermore accelerated $O_2$ reduction to generate ·OOH as indicated by the in-situ EPR and NBT photodegradation results. Simultaneously $H_2O$ oxidation to ·OH was greatly enhanced by the Au cocatalyst, then promoting $CH_4$ activation and suppressing over-oxidation. Isotopic measurement evidenced $O_2$ was the only oxygen source for oxygenates generation, while $H_2O$ as a promoter for $CH_4$ activation. This work broadened the design and understanding of binary cocatalysts on simultaneous activity increase and selectivity regulation to achieve highly selective photocatalytic methane conversion to high-value-added chemicals.

## ASSOCIATED CONTENT

### Supporting information

Supporting information is available free of charge on the ACS publications.

Detailed experimental procedures, characterizations, control experiments, additional reactions, and characterization data (Figure S1-22 and Table S1-3).

## CONFLICTS OF INTEREST

There are no conflicts to declare.

**ACKNOWLEDGEMENTS**

L. L., Z. G., J. M., H. L. and J. X., are thankful for the China Postdoctoral Science Foundation (Grant No. 2019M663802), the National Natural Science Foundation of China (21973075) and the Shannxi Key Research Grant (China, 2020GY-244). Y. X. and J.T., are thankful for financial support from the UK EPSRC (EP/S018204/2), Leverhulme Trust (RPG-2017-122), Royal Society Newton Advanced Fellowship grant (NAF\R1\191163 and NA170422) and Royal Society Leverhulme Trust Senior Research Fellowship (SRF\R1\21000153).

**REFERENCES**

[1] Saha, D., H.A. Grappe, A. Chakraborty, and G. Orkoulas. Postextraction Separation, on-Board Storage, and Catalytic Conversion of Methane in Natural Gas: A Review. *Chem. Rev.*, **2016**, *116*, 11436.

[2] Ab Rahim, M.H., M.M. Forde, R.L. Jenkins, C. Hammond, Q. He, N. Dimitratos, J.A. Lopez-Sanchez, A.F. Carley, S.H. Taylor, D.J. Willock, D.M. Murphy, C.J. Kiely, and G.J. Hutchings. Oxidation of Methane to Methanol with Hydrogen Peroxide Using Supported Gold-Palladium Alloy Nanoparticles. *Angew. Chem. Int. Ed.*, **2013**, *52*, 1280.

[3] Ravi, M., M. Ranocchiari, and J.A. van Bokhoven. The Direct Catalytic Oxidation of Methane to Methanol-a Critical Assessment. *Angew. Chem. Int. Ed.*, **2017**, *56*, 16464.

[4] Song, H., X. Meng, Z.-j. Wang, H. Liu, and J. Ye. Solar-Energy-Mediated Methane Conversion. *Joule*, **2019**, *3*, 1606.

[5] Cui, X., H. Li, Y. Wang, Y. Hu, L. Hua, H. Li, X. Han, Q. Liu, F. Yang, L. He, X. Chen, Q. Li, J. Xiao, D. Deng, and X. Bao. Room-Temperature Methane Conversion by Graphene-Confined Single Iron Atoms. *Chem*, **2018**, *4*, 1902.

[6] Jin, Z., L. Wang, E. Zuidema, K. Mondal, M. Zhang, J. Zhang, C. Wang, X. Meng, H. Yang, C. Mesters, and F.-S. Xiao. Hydrophobic Zeolite Modification for in Situ Peroxide Formation in Methane Oxidation to Methanol. *Science*, **2020**, *367*, 193.

[7] Sushkevich, V.L., D. Palagin, M. Ranocchiari, and J.A.v. Bokhoven. Selective Anaerobic Oxidation of Methane Enables Direct Synthesis of Methanol. *Science*, **2017**, *356*, 523.

[8] Ravi, M., V.L. Sushkevich, A.J. Knorpp, M.A. Newton, D. Palagin, A.B. Pinar, M. Ranocchiari,

and J.A. van Bokhoven. Misconceptions and Challenges in Methane-to-Methanol over Transition-Metal-Exchanged Zeolites. *Nat. Catal.*, **2019**, *2*, 485.

[9] Hu, D., V.V. Ordomsky, and A.Y. Khodakov. Major Routes in the Photocatalytic Methane Conversion into Chemicals and Fuels under Mild Conditions. *Appl. Catal. B-Environ.*, **2021**, *286*, 119913.

[10] Liu, Y., D. Deng, and X. Bao. Catalysis for Selected C1 Chemistry. *Chem*, **2020**, *6*, 2497.

[11] Tian, Y., L. Piao, and X. Chen. Research Progress on the Photocatalytic Activation of Methane to Methanol. *Green Chem.*, **2021**, *23*, 3526.

[12] Jin, R., M. Peng, A. Li, Y. Deng, Z. Jia, F. Huang, Y. Ling, F. Yang, H. Fu, J. Xie, X. Han, D. Xiao, Z. Jiang, H. Liu, and D. Ma. Low Temperature Oxidation of Ethane to Oxygenates by Oxygen over Iridium-Cluster Catalysts. *J. Am. Chem. Soc.*, **2019**, *141*, 18921.

[13] Zhang, H., C. Li, Q. Lu, M.-J. Cheng, and W.A. Goddard. Selective Activation of Propane Using Intermediates Generated During Water Oxidation. *J. Am. Chem. Soc.*, **2021**, *143*, 3967.

[14] Simons, M.C., S.D. Prinslow, M. Babucci, A.S. Hoffman, J. Hong, J.G. Vitillo, S.R. Bare, B.C. Gates, C.C. Lu, L. Gagliardi, and A. Bhan. Beyond Radical Rebound: Methane Oxidation to Methanol Catalyzed by Iron Species in Metal-Organic Framework Nodes. *J. Am. Chem. Soc.*, **2021**, *143*, 12165.

[15] Agarwal, N., S.J. Freakley, R.U. McVicker, S.M. Althahban, N. Dimitratos, Q. He, D.J. Morgan, R.L. Jenkins, D.J. Willock, S.H. Taylor, C.J. Kiely, and G.J. Hutchings. Aqueous Au-Pd Colloids Catalyze Selective $CH_4$ Oxidation to $CH_3OH$ with $O_2$ under Mild Conditions. *Science*, **2017**, *358*, 223.

[16] Wu, X., Y. Zeng, H. Liu, J. Zhao, T. Zhang, and S.L. Wang. Noble-Metal-Free Dye-Sensitized Selective Oxidation of Methane to Methanol with Green Light (550 nm). *Nano Res.*, **2021**, *14*, 4584.

[17] Luo, L., J. Luo, H. Li, F. Ren, Y. Zhang, A. Liu, W.X. Li, and J. Zeng. Water Enables Mild Oxidation of Methane to Methanol on Gold Single-Atom Catalysts. *Nat. Commun.*, **2021**, *12*, 1218.

[18] Grundner, S., M.A. Markovits, G. Li, M. Tromp, E.A. Pidko, E.J. Hensen, A. Jentys, M. Sanchez-Sanchez, and J.A. Lercher. Single-Site Trinuclear Copper Oxygen Clusters in Mordenite for Selective Conversion of Methane to Methanol. *Nat. Commun.*, **2015**, *6*, 7546.

[19] Agarwal, N., S.J. Freakley, R.U. McVicker, S.M. Althahban, N. Dimitratos, Q. He, D.J. Morgan, R.L. Jenkins, D.J. Willock, S.H. Taylor, C.J. Kiely, and G.J. Hutchings. Aqueous Au-Pd Colloids Catalyze Selective $CH_4$ Oxidation to $CH_3OH$ with $O_2$ under Mild Conditions. *Science*, **2017**, *358*, 223.

[20] Ghosh, I., J. Khamrai, A. Savateev, N. Shlapakov, M. Antonietti, and B. König. Organic Semiconductor Photocatalyst Can Bifunctionalize Arenes and Heteroarenes. *Science*, **2019**, *365*, 360.

[21] Kumar, S.G. and L.G. Devi. Review on Modified $TiO_2$ Photocatalysis under UV/Visible Light: Selected Results and Related Mechanisms on Interfacial Charge Carrier Transfer Dynamics. *J Phys. Chem. A*, **2011**, *115*, 13211.

[22] Lee, B.-H., S. Park, M. Kim, A.K. Sinha, S.C. Lee, E. Jung, W.J. Chang, K.-S. Lee, J.H. Kim, S.-P. Cho, H. Kim, K.T. Nam, and T. Hyeon. Reversible and Cooperative Photoactivation of Single-Atom Cu/$TiO_2$ Photocatalysts. *Nat. Mater.*, **2019**, *18*, 620.

[23] Oshima, T., S. Nishioka, Y. Kikuchi, S. Hirai, K.-i. Yanagisawa, M. Eguchi, Y. Miseki, T. Yokoi, T. Yui, K. Kimoto, K. Sayama, O. Ishitani, T.E. Mallouk, and K. Maeda. An Artificial Z-Scheme Constructed from Dye-Sensitized Metal Oxide Nanosheets for Visible Light-Driven Overall Water Splitting. *J. Am. Chem. Soc.*, **2020**, *142*, 8412.

[24] Ulmer, U., T. Dingle, P.N. Duchesne, R.H. Morris, A. Tavasoli, T. Wood, and G.A. Ozin. Fundamentals and Applications of Photocatalytic $CO_2$ Methanation. *Nat. Commun.*, **2019**, *10*, 3169.

[25] Zhu, S., X. Li, Z. Pan, X. Jiao, K. Zheng, L. Li, W. Shao, X. Zu, J. Hu, J. Zhu, Y. Sun, and Y. Xie. Efficient Photooxidation of Methane to Liquid Oxygenates over ZnO Nanosheets at Atmospheric Pressure and near Room Temperature. *Nano Lett.*, **2021**, *21*, 4122.

[26] Sun, Z., C. Wang, and Y.H. Hu. Highly Selective Photocatalytic Conversion of Methane to Liquid Oxygenates over Silicomolybdic-Acid/$TiO_2$ under Mild Conditions. *J. Mater. Chem. A*, **2021**, *2021*, 1713.

[27] Villa, K., S. Murcia-López, J.R. Morante, and T. Andreu. An Insight on the Role of La in Mesoporous $WO_3$ for the Photocatalytic Conversion of Methane into Methanol. *Appl. Catal. B-Environ.*, **2016**, *187*, 30.

[28] Yang, J., J. Hao, J. Wei, J. Dai, and Y. Li. Visible-Light-Driven Selective Oxidation of Methane to Methanol on Amorphous FeOOH Coupled M-$WO_3$. *Fuel*, **2020**, *266*, 117104.

[29] Zhou, W., X. Qiu, Y. Jiang, Y. Fan, S. Wei, D. Han, L. Niu, and Z. Tang. Highly Selective Aerobic Oxidation of Methane to Methanol over Gold Decorated Zinc Oxide Via Photocatalysis. *J. Mater. Chem. A*, **2020**, *8*, 13277.

[30] Rosenthal, J., T.D. Luckett, J.M. Hodgkiss, and D.G. Nocera. Photocatalytic Oxidation of Hydrocarbons by a Bis-Iron(Iii)-M-Oxo Pacman Porphyrin Using $O_2$ and Visible Light. *J. Am. Chem. Soc.*, **2006**, *128*, 6546.

[31] Xie, J., R. Jin, A. Li, Y. Bi, Q. Ruan, Y. Deng, Y. Zhang, S. Yao, G. Sankar, D. Ma, and J. Tang. Highly Selective Oxidation of Methane to Methanol at Ambient Conditions by Titanium Dioxide-Supported Iron Species. *Nat. Catal.*, **2018**, *1*, 889.

[32] Song, H., X. Meng, S. Wang, W. Zhou, X. Wang, T. Kako, and J. Ye. Direct and Selective Photocatalytic Oxidation of $CH_4$ to Oxygenates with $O_2$ on Cocatalysts/ZnO at Room Temperature in Water. *J. Am. Chem. Soc.*, **2019**, *141*, 20507.

[33] Wei, S., X. Zhu, P. Zhang, Y. Fan, Z. Sun, X. Zhao, D. Han, and L. Niu. Aerobic Oxidation of Methane to Formaldehyde Mediated by Crystal-O over Gold Modified Tungsten Trioxide Via Photocatalysis. *Appl. Catal. B-Environ.*, **2021**, *283*, 119661.

[34] Fan, Y., W. Zhou, X. Qiu, H. Li, Y. Jiang, Z. Sun, D. Han, L. Niu, and Z. Tang. Selective Photocatalytic Oxidation of Methane by Quantum-Sized Bismuth Vanadate. *Nat. Sustain.*, **2021**, *4*, 509.

[35] Yu, X., V.L. Zholobenko, S. Moldovan, D. Hu, D. Wu, V.V. Ordomsky, and A.Y. Khodakov. Stoichiometric Methane Conversion to Ethane Using Photochemical Looping at Ambient Temperature. *Nature Energy*, **2020**, *5*, 511.

[36] Li, X., J. Xie, H. Rao, C. Wang, and J. Tang. Pt and Cuox Decorated $TiO_2$ Photocatalyst for Oxidative Coupling of Methane to $C_2$ Hydrocarbons in a Flow Reactor. *Angew. Chem. Int. Ed.*, **2020**, *59*, 19702.

[37] Ishimaru, M., F. Amano, C. Akamoto, and S. Yamazoe. Methane Coupling and Hydrogen Evolution Induced by Palladium-Loaded Gallium Oxide Photocatalysts in the Presence of Water Vapor. *J. Catal.*, **2021**, *397*, 192.

[38] Yu, L., Y. Shao, and D. Li. Direct Combination of Hydrogen Evolution from Water and Methane Conversion in a Photocatalytic System over Pt/$TiO_2$. *Appl. Catal. B-Environ.*, **2017**, *204*, 216.

[39] Chen, Z., S. Wu, J. Ma, S. Mine, T. Toyao, M. Matsuoka, L. Wang, and J. Zhang. Non‐Oxidative Coupling of Methane: n-type Doping of Niobium Single Atoms in $TiO_2$-$SiO_2$ Induces Electron Localization. *Angew. Chem. Int. Ed.*, **2021**, *60*, 11901.

[40] Zhou, Y., L. Zhang, and W. Wang. Direct Functionalization of Methane into Ethanol over Copper Modified Polymeric Carbon Nitride Via Photocatalysis. *Nat. Commun.*, **2019**, *10*, 506.

[41] Trang, T.N.Q., T.B. Phan, N.D. Nam, and V.T.H. Thu. In Situ Charge Transfer at the Ag@ZnO Photoelectrochemical Interface toward the High Photocatalytic Performance of H2 Evolution and RhB Degradation. *ACS Appl. Mater. Inter.*, **2020**, *12*, 12195.

[42] Cui, X., Y. Chen, M. Zhang, Y.W. Harn, J. Qi, L. Gao, Z.L. Wang, J. Huang, Y. Yang, and Z. Lin. Tailoring Carrier Dynamics in Perovskite Solar Cells Via Precise Dimension and Architecture Control and Interfacial Positioning of Plasmonic Nanoparticles. *Energy Environ. Sci.*, **2020**, *13*, 1743.

[43] Song, H., X. Meng, S. Wang, W. Zhou, S. Song, T. Kako, and J. Ye. Selective Photo-Oxidation of Methane to Methanol with Oxygen over Dual-Cocatalyst-Modified Titanium Dioxide. *ACS Catal.*, **2020**, *10*, 14318.

[44] Liu, X., M.-H. Liu, Y.-C. Luo, C.-Y. Mou, S.D. Lin, H. Cheng, J.-M. Chen, J.-F. Lee, and T.-S. Lin. Strong Metal–Support Interactions between Gold Nanoparticles and ZnO Nanorods in CO Oxidation. *J. Am. Chem. Soc.*, **2012**, *134*, 10251.

[45] Qin, R., K. Liu, Q. Wu, and N. Zheng. Surface Coordination Chemistry of Atomically Dispersed Metal Catalysts. *Chem. Rev.*, **2020**, *120*, 11810.

[46] Zhang, W., H. Wang, J. Jiang, Z. Sui, Y. Zhu, D. Chen, and X. Zhou. Size Dependence of Pt Catalysts for Propane Dehydrogenation: From Atomically Dispersed to Nanoparticles. *ACS Catal.*, **2020**, *10*, 12932.

[47] Zhang, Y., X. Su, L. Li, H. Qi, C. Yang, W. Liu, X. Pan, X. Liu, X. Yang, Y. Huang, and T. Zhang. $Ru/TiO_2$ Catalysts with Size-Dependent Metal/Support Interaction for Tunable Reactivity in Fischer–Tropsch Synthesis. *ACS Catal.*, **2020**, *10*, 12967.

[48] Jeong, H., S. Shin, and H. Lee. Heterogeneous Atomic Catalysts Overcoming the Limitations of Single-Atom Catalysts. *ACS Nano*, **2020**, *14*, 14355.

[49] Kwon, Y., T.Y. Kim, G. Kwon, J. Yi, and H. Lee. Selective Activation of Methane on Single-Atom Catalyst of Rhodium Dispersed on Zirconia for Direct Conversion. *J. Am. Chem. Soc.*, **2017**, *139*, 17694.

[50] Blankenship, A.N., M. Ravi, M.A. Newton, and J.A. van Bokhoven. Heterogeneously Catalyzed Aerobic Oxidation of Methane to a Methyl Derivative. *Angew. Chem. Int. Ed.*, **2021**, *60*, 18138.

[51] Latimer, A.A., A. Kakekhani, A.R. Kulkarni, and J.K. Nørskov. Direct Methane to Methanol: The Selectivity–Conversion Limit and Design Strategies. *ACS Catal.*, **2018**, *8*, 6894.

[52] Lustemberg, P.G., R.M. Palomino, R.A. Gutiérrez, D.C. Grinter, M. Vorokhta, Z. Liu, P.J. Ramírez, V. Matolín, M.V. Ganduglia-Pirovano, S.D. Senanayake, and J.A. Rodriguez. Direct Conversion of Methane to Methanol on Ni-Ceria Surfaces: Metal–Support Interactions and Water-Enabled Catalytic Conversion by Site Blocking. *J. Am. Chem. Soc.*, **2018**, *140*, 7681.

[53] Long, R., Y. Li, Y. Liu, S. Chen, X. Zheng, C. Gao, C. He, N. Chen, Z. Qi, L. Song, J. Jiang, J.

Zhu, and Y. Xiong. Isolation of Cu Atoms in Pd Lattice: Forming Highly Selective Sites for Photocatalytic Conversion of $CO_2$ to $CH_4$. *J. Am. Chem. Soc.*, **2017**, *139*, 4486.

[54] Han, C., M.-Q. Yang, N. Zhang, and Y.-J. Xu. Enhancing the Visible Light Photocatalytic Performance of Ternary CdS-(Graphene-Pd) Nanocomposites Via a Facile Interfacial Mediator and Co-Catalyst Strategy. *J. Mater. Chem. A*, **2014**, *2*, 19156.

[55] Wu, X.Y., Z. Tang, X. Zhao, X. Luo, S. John Pennycook, and S.L. Wang. Visible-Light Driven Room-Temperature Coupling of Methane to Ethane by Atomically Dispersed Au on $WO_3$. *Journal of Energy Chemistry*, **2021**, *61*, 195.

[56] Chiu, Y.-H., K.-D. Chang, and Y.-J. Hsu. Plasmon-Mediated Charge Dynamics and Photoactivity Enhancement for Au-Decorated ZnO Nanocrystals. *J. Mater. Chem. A*, **2018**, *6*, 4286.

[57] Tada, H., T. Mitsui, T. Kiyonaga, T. Akita, and K. Tanaka. All-Solid-State Z-Scheme in CdS-Au-$TiO_2$ Three-Component Nanojunction System. *Nat. Mater.*, **2006**, *5*, 782.

[58] Dinh, K.T., M.M. Sullivan, P. Serna, R.J. Meyer, M. Dincă, and Y. Román-Leshkov. Viewpoint on the Partial Oxidation of Methane to Methanol Using Cu- and Fe-Exchanged Zeolites. *ACS Catal.*, **2018**, *8*, 8306.

[59] Geng, M. and Z. Duan. Prediction of Oxygen Solubility in Pure Water and Brines up to High Temperatures and Pressures. *Geochimica et Cosmochimica Acta*, **2010**, *74*, 5631.

[60] Liu, C.-C., H.-J. Chou, C.-Y. Lin, D. Janmanchi, P.-W. Chung, C.-Y. Mou, S.S.F. Yu, and S.I. Chan. The Oversolubility of Methane Gas in Nano-Confined Water in Nanoporous Silica Materials. *Micropor. Mesopor. Mat.*, **2020**, *293*, 109793.

[61] Xu, C.Y., P.X. Zhang, and L. Yan. Blue Shift of Raman Peak from Coated $TiO_2$ Nanoparticles. *J. Raman Spectrosc.*, **2001**, *32*, 862.

[62] Nadupalli, S., S. Repp, S. Weber, and E. Erdem. About Defect Phenomena in ZnO Nanocrystals. *Nanoscale*, **2021**, *13*, 9160.

[63] Cerrato, E., M.C. Paganini, and E. Giamello. Photoactivity under Visible Light of Defective ZnO Investigated by EPR Spectroscopy and Photoluminescence. *J. Photochem. Photobiol., A*, **2020**, *397*, 112531.

[64] Sterrer, M., O. Diwald, E. Kno1zinger, P.V. Sushko, and A.L. Shluger. Energies and Dynamics of Photoinduced Electron and Hole Processes on Mgo Powders. *J. Phys. Chem. B*, **2002**, *106*, 12478.

[65] Li, G., N.M. Dimitrijevic, L. Chen, T. Rajh, and K.A. Gray. Role of Surface/Interfacial $Cu^{2+}$ Sites in the Photocatalytic Activity of Coupled CuO-$TiO_2$ Nanocomposites. *J. Phys. Chem. C*, **2008**,

*112*, 19040.

[66] Huang, J., L. Dou, J. Li, J. Zhong, M. Li, and T. Wang. Excellent Visible Light Responsive Photocatalytic Behavior of N-Doped $TiO_2$ toward Decontamination of Organic Pollutants. *J. Hazard. Mater.*, **2021**, *403*, 123857.

[67] Xiong, L. and J. Tang. Strategies and Challenges on Selectivity of Photocatalytic Oxidation of Organic Substances. *Adv. Energy Mater.*, **2021**, *11*, 2003216.

[68] Wang, K., Y. Li, G. Zhang, J. Li, and X. Wu. 0D Bi Nanodots/2D $Bi_3NbO_7$ Nanosheets Heterojunctions for Efficient Visible Light Photocatalytic Degradation of Antibiotics: Enhanced Molecular Oxygen Activation and Mechanism Insight. *Appl. Catal. B-Environ.*, **2019**, *240*, 39.

[69] Ai, S., Q. Wang, H. Li, and L. Jin. Study on Production of Free Hydroxyl Radical and Its Reaction with Salicylic Acid at Lead Dioxide Electrode. *J. Electroanal. Chem.*, **2005**, *578*, 223.

[70] Wu, X., K. Tan, Z. Tang, and X. Lu. Hydrogen Bonding in Microsolvation: Photoelectron Imaging and Theoretical Studies on Au(X)(-)-(H2o)(N) and Au(X)(-)-(CH3OH)(N) (X = 1, 2; N = 1, 2) Complexes. *Phys. Chem. Chem. Phys.*, **2014**, *16*, 4771.

[71] Xing, B. and G.-C. Wang. Insight into the General Rule for the Activation of the X–H Bonds (X = C, N, O, S) Induced by Chemisorbed Oxygen Atoms. *Phys. Chem. Chem. Phys.*, **2014**, *16*, 2621.

[72] Schneider, J. and D.W. Bahnemann. Undesired Role of Sacrificial Reagents in Photocatalysis. *J Phys. Chem. Lett.*, **2013**, *4*, 3479.

**TOC Graphic：**

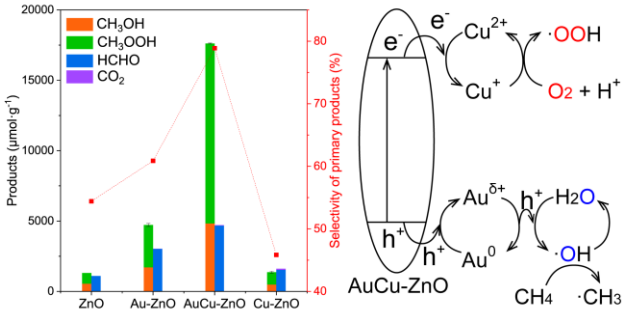
CH3OH
CH3OOH
HCHO
CO2
Products (μmol·g-1)
Selectivity of primary products (%)
ZnO
Au-ZnO
AuCu-ZnO
Cu-ZnO
e-
h+
Cu2+
Cu+
·OOH
O2 + H+
Auδ+
Au0
H2O
·OH
CH4
·CH3
AuCu-ZnO